Influence of Mono- and Bimetallic PtO$_x$, PdO$_x$, PtPdO$_x$ Clusters on CO Sensing by SnO$_2$ Based Gas Sensors

Pavel Kutukov [1], Marina Rumyantseva [1,*], Valeriy Krivetskiy [1], Darya Filatova [1], Maria Batuk [2], Joke Hadermann [2], Nikolay Khmelevsky [3], Anatoly Aksenenko [3] and Alexander Gaskov [1,*]

[1] Chemistry Department, Moscow State University, 119991 Moscow, Russia; spamflame@gmail.com (P.K.); vkrivetsky@gmail.com (V.K.); gak1.analyt@gmail.com (D.F.)

[2] EMAT, University of Antwerp, B-2020 Antwerp, Belgium; maria.batuk@uantwerpen.be (M.B.); Joke.Hadermann@uantwerpen.be (J.H.)

[3] LISM, Moscow State Technological University Stankin, 127055 Moscow, Russia; khmelevsky@mail.ru (N.K.); a.aksenenko@lism-stankin.ru (A.A.)

* Correspondence: roum@inorg.chem.msu.ru (M.R.); gaskov@inorg.chem.msu.ru (A.G.); Tel.: +7-495-939-5471 (M.R. & A.G.)

check for updates

Abstract: To obtain a nanocrystalline SnO$_2$ matrix and mono- and bimetallic nanocomposites SnO$_2$/Pd, SnO$_2$/Pt, and SnO$_2$/PtPd, a flame spray pyrolysis with subsequent impregnation was used. The materials were characterized using X-ray diffraction (XRD), a single-point BET method, transmission electron microscopy (TEM), and high angle annular dark field scanning transmission electron microscopy (HAADF-STEM) with energy dispersive X-ray (EDX) mapping. The electronic state of the metals in mono- and bimetallic clusters was determined using X-ray photoelectron spectroscopy (XPS). The active surface sites were investigated using the Fourier Transform infrared spectroscopy (FTIR) and thermo-programmed reduction with hydrogen (TPR-H$_2$) methods. The sensor response of blank SnO$_2$ and nanocomposites had a carbon monoxide (CO) level of 6.7 ppm and was determined in the temperature range 60–300 °C in dry (Relative Humidity (RH) = 0%) and humid (RH = 20%) air. The sensor properties of the mono- and bimetallic nanocomposites were analyzed on the basis of information on the electronic state, the distribution of modifiers in SnO$_2$ matrix, and active surface centers. For SnO$_2$/PtPd, the combined effect of the modifiers on the electrophysical properties of SnO$_2$ explained the inversion of sensor response from *n*- to *p*-types observed in dry conditions.

Keywords: nanocrystalline semiconductor oxides; nanocomposites; tin oxide; platinum; palladium; bimetallic particles; carbon monoxide; gas sensor; response inversion

1. Introduction

Because SnO$_2$ is a wide-bandgap oxygen-deficient *n*-type semiconductor with optical transparency, electron conductivity, and a high specific surface area, it is suitable for a large range of applications, including in solar cells, as catalytic support, and as solid state gas sensors [1]. However, the use of bare SnO$_2$ is often limited by lack of selectivity and a high operating temperature [2]. Chemical modification is a well-established practice intended to solve those problems [2–5]. This involves the creation of new active sites, with specific adsorptivity and reactivity toward target gases (i.e., carbon monoxide), on the surface of a semiconductor matrix.

Carbon monoxide (CO) is a colorless, odorless, and tasteless toxic gas, produced by automotive emissions, natural gas manufacturing, industrial activities, and the incomplete burning of fuels [6]. In the

human body, it reacts readily with hemoglobin to form carboxyhemoglobin. Carbon monoxide exposure is still one of the leading causes of unintentional and suicidal poisonings, and it causes a large number of deaths annually. [7] Thus, real-time monitoring of CO is extremely important for safety reasons.

Carbon monoxide is a reducing gas without pronounced acid or basic properties [3]. To enhance the sensor signal of a SnO_2 based sensor toward such gases, the catalytically active additives metallic platinum, gold, and silver are the most effective [6,8]. These modifiers take part in the oxidation of CO on the surface of the semiconductor oxide and lead to a change in the type and concentration of active groups on that surface [5]. This not only leads to an increased sensor response, but also to a decrease in temperature, at which a maximum sensitivity is observed [2–5]. The selectivity of heterogeneous catalysts of oxidative processes is determined by the energy of adsorption of the reducing gas, the binding energy with surface oxygen (which is an oxidizer) and binding energies with intermediates and reaction products. In CO oxidation, the optimal catalysts are palladium (Pd) and platinum (Pt), since the energy of chemisorption of oxygen on the clusters of these metals (340–360 kJ/mol) is close to the binding energy of CO with their surface [9,10]. Palladium and platinum are some of the most effective modifiers for improving the sensor properties of semiconductor metal oxides in CO detection [11–27].

The properties of bimetallic catalysts are now being actively investigated due to the expected synergistic effect—i.e., that the activity of the bimetallic catalyst exceeds the sum of the activities of its monometallic analogues [28–40]. In gas sensors, it is thought that the surface modification of semiconductor oxides with bimetallic catalysts should create optimal conditions for both electron and ion exchange (spillover effect) between the surface nanoclusters and the metal oxide support [41]. As bimetallic catalytically active modifiers for gas sensors, nanoparticles that contain platinum group metals in various combinations are usually studied, as well as Au and *d*-elements such as Fe, Co, Ni, and Cu [42–52]. Despite the fact that numerous monometallic systems have already been studied, including SnO_2/Pt and SnO_2/Pd, only a few reports on CO sensing properties of bimetallic SnO_2/PtPd nanocomposite are known [44,52].

The procedure of conventional and widespread wet-chemical synthesis of nanocrystalline SnO_2 is well-known and relatively simple [53]. However, this method is rather time-consuming, as the hydrated SnO_2 needs to be repeatedly washed. Flame spray pyrolysis (FSP) is an alternative method for producing metal oxides for catalysts and semiconductor gas sensors [54–56]. The advantage of the FSP method is the ability to produce highly dispersed materials with nanometer-sized crystallites that have high crystallinity and porosity. The use of precursors of the main components and modifiers during the one-stage synthesis allows for the obtainment of a modified material with the necessary set of functional properties regarding the specific surface area, electrical conductivity, acid-base, and oxidation-reduction ability in interaction with gases [17,57–64].

In this study, the nanocrystalline SnO_2 matrix was synthesized using FSP. Mono- and bimetallic nanocomposites SnO_2/Pd, SnO_2/Pt, and SnO_2/PtPd were then obtained via impregnation. The sample characteristics are presented in Table 1. The gas sensing properties of the bimetallic nanocomposite SnO_2/PtPd were compared to those of the monometallic nanocomposites SnO_2/Pt and SnO_2/Pd and analyzed on the basis of information on the Pt and Pd electronic state, the distribution of modifiers in the SnO_2 matrix, and the type and concentration of active centers on the surface of the nanocomposites.

Table 1. Microstructure characteristics and composition of investigated samples.

Sample	S_{surf}, m²/g	d_{XRD} (SnO_2), nm [a]	d_{TEM}, nm [b]			[M], wt.% [c]
			SnO_2	Pd	Pt	
SnO_2				-	-	-
SnO_2/Pd				<2; 8–20	-	1.5 ± 0.2 [c]
SnO_2/Pt	22 ± 5	10 ± 1	10.7 ± 4.9	-	25–100	1.0 ± 0.2 [c]
SnO_2/PtPd				<2	17–64	1.3 ± 0.2 (Pd) 0.3 ± 0.1 (Pt)

[a] crystallite size (X-ray diffraction, XRD); [b] particle size (transmission electron microscopy, TEM); [c] obtained using X-ray fluorescence (XRF) analysis.

2. Results and Discussion

Figure 1 shows the change in the resistance of the samples in the temperature range 60–300 °C under periodic change of the gas phase composition: air (15 min), 6.7 ppm CO in air (15 min). The measurements were effectuated in dry air (Relative Humidity (RH) = 0%, Figure 1a) and humid air (RH = 20%, Figure 1b). The decrease in the electrical resistance in the presence of CO (*n*-type response) was due to the oxidation of carbon monoxide by chemisorbed oxygen:

$$\beta \cdot CO_{(gas)} + O_{\beta(ads)}^{-\alpha} \leftrightarrow \beta \cdot CO_{2(gas)} + \alpha \cdot e^{-} \tag{1}$$
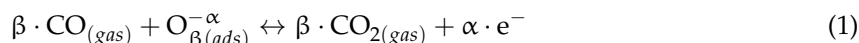
where $CO_{(gas)}$ represents the carbon monoxide molecule in the gas phase, $O_{\beta(ads)}^{-\alpha}$ is chemisorbed oxygen, $CO_{2(gas)}$ is the reaction product desorbed to the gas phase, and e is an electron injected into the conduction band of the *n*-type semiconductor. The sensor signal for *n*-type response was calculated for each temperature as $S = \frac{\Delta G}{G_{air}} = \frac{G_{gas} - G_{air}}{G_{air}}$, where G_{air} is the sample's conductance in air and G_{gas} is the sample's conductance in the presence of 6.7 ppm CO in air (Figure 2). For $SnO_2/PtPd$ nanocomposite the increase in the electrical resistance in the presence of CO (*p*-type response) was observed in the temperature range 150–300 °C at RH = 0% (Figure 1c). In these cases, the sensor signal was calculated as $S = \frac{\Delta R}{R_{air}} = \frac{R_{gas} - R_{air}}{R_{air}}$, where R_{air} is the sample's resistance in air and R_{gas} is the sample's resistance in the presence of 6.7 ppm CO in air.
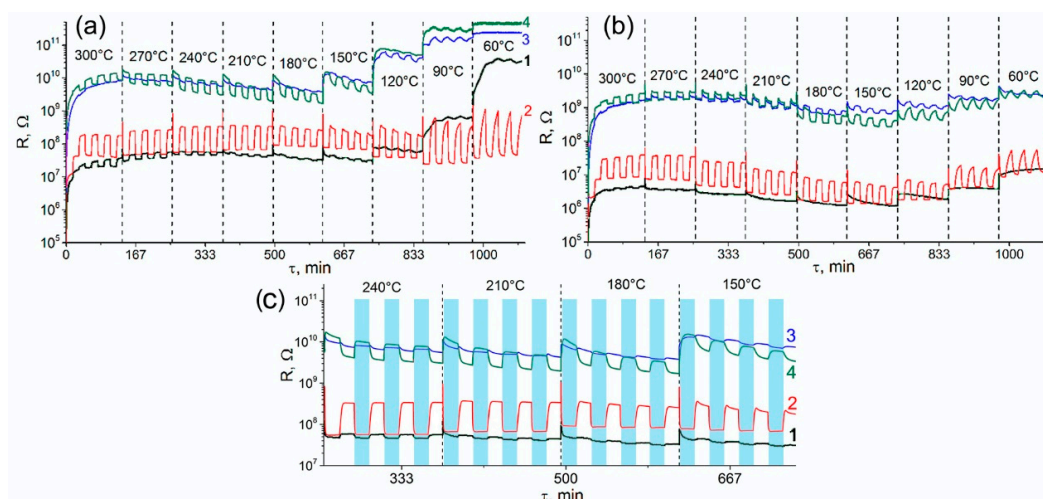
Figure 1. Resistance of the samples in the temperature range 60–300 °C under the periodic change of the gas phase composition at relative humidity (**a**) Relative Humidity (RH) = 0% and (**b**) RH = 20%. (**c**) An enlarged image of the resistance variation of the samples when measured in dry air (RH = 0%). (1) SnO_2, (2) SnO_2/Pd, (3) SnO_2/Pt, (4) $SnO_2/PtPd$. Pale blue areas correspond to exposure in CO.
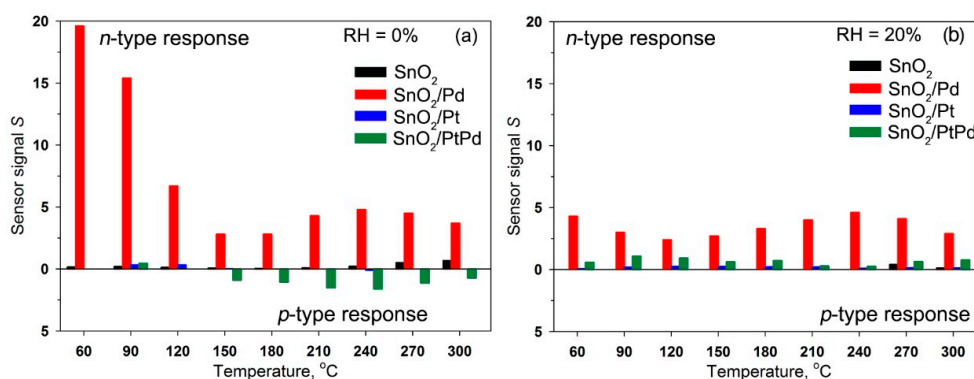

Figure 2. Sensor signal to 6.7 ppm CO of blank SnO_2 and mono- and bimetallic nanocomposites in the temperature range 60–300 °C at relative humidity RH = 0% (**a**) and RH = 20% (**b**).

The data presented in Figures 1 and 2, revealed the following trends.

(i) Comparison of the resistance values show that the introduction of modifiers caused an increase in the resistance of tin dioxide. This effect was most pronounced for nanocomposites containing platinum.

(ii) For the non-modified SnO_2, the value of the *n*-type sensor response toward CO increased with increasing measurement temperature and reached a maximum at 270–300 °C. The increase in humidity almost completely suppressed the sensor response of SnO_2 sample.

(iii) For the SnO_2/Pd nanocomposite, only the *n*-type response was observed. Two maxima can be distinguished on the temperature dependence of the sensor signal: one in the temperature range 240–270 °C and one in the range 60–90 °C. The sensor signal values at 240–270 °C decreased slightly with increasing air humidity from RH = 0% to RH = 20%. In the low-temperature interval, an increase in humidity led to a significant decrease in the sensor signal.

(iv) The SnO_2/Pt nanocomposite exhibited a low sensor response. However, in the low-temperature range, its response to CO in dry air exceeded the analogous value for unmodified SnO_2, while in the high-temperature region its sensor signal turns out to be lower than for SnO_2. The inversion of the sensor response from the *n*-type to the *p*-type is observed only when measured in dry air at T = 240 °C.

(v) When performing the measurements in dry air, the inversion of the sensor response was characteristic for bimetallic nanocomposite SnO_2/PtPd over a wide temperature range. The maximum of the *p*-type response was observed at 210–240 °C. The increase in air humidity led to the disappearance of the inversion of the response. The observed *n*-type response in the whole temperature range was lower than for palladium containing monometallic nanocomposite SnO_2/Pd.

To determine the factors responsible for the formation of the sensor response of mono- and bimetallic nanocomposites, the phase composition, the electronic state of platinum and palladium, and their distribution in the SnO_2 matrix were investigated. The effect of the presence of various modifiers on the surface composition of nanocrystalline SnO_2 was studied in detail.

The X-ray diffraction (XRD) pattern of SnO_2 corresponds to the cassiterite phase (ICDD 41-1445, Figure 3). The introduction of catalytic modifiers did not led to a change in the phase composition of the samples. The reflections corresponding to Pt- or Pd-containing phases do not appear on the diffractograms of the nanocomposites.
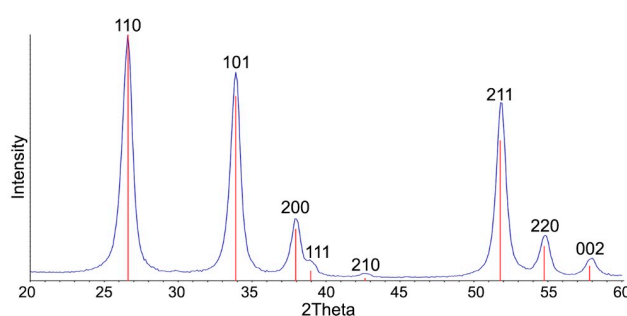

Figure 3. X-ray diffraction (XRD) pattern of SnO_2 powder obtained using the flame spray pyrolysis (FSP) method. Vertical lines correspond to the ICDD 41-1445 reference (SnO_2 cassiterite).

According to the high angle annular dark field scanning transmission electron microscopy (HAADF-STEM) images, all the materials were composed of agglomerated crystalline SnO_2 nanoparticles, with sizes varying from approximately 5–35 nm, with an average size of 10.7 ± 4.9 nm (Figure 4). The introduction of modifiers does not affect the particle size of SnO_2. In SnO_2/Pd nanocomposite (Figure 5) several Pd particles with a size 8–20 nm were found among the SnO_2 matrix particles (Figure 5b). Also small Pd particles with a size of 2 nm could be seen on the images and energy dispersive X-ray (EDX) maps (Figure 5b).

In the SnO_2/Pt nanocomposite, the Pt particles were very easy to see on the HAADF-STEM images (Figure 6a) because they are large and bright. Their size varied in the range of 25–100 nm and the average size was 49.1 ± 19.5 nm (Figure 6c).

The nanocomposite SnO_2/PtPd contained bimetallic nanoparticles particles, which were present in a form of agglomerates with the size 17–64 nm (Figure 7). According to the EDX maps, the particles contained both metals (Figure 7b), however their ratio varied from particle to particle and was independent from the particle size (Figure 7c). The distribution of Pt and Pd inside the particle was not uniform. Besides the PtPd particles, small Pd particles with a size about 2 nm could be seen on the maps (Figure 7b).
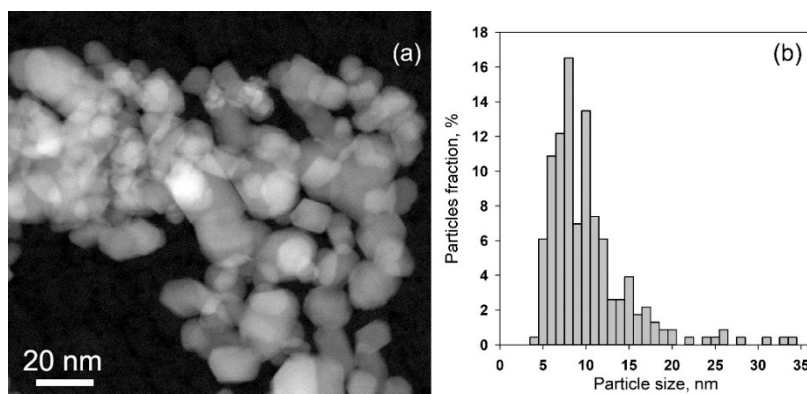

Figure 4. High angle annular dark field scanning transmission electron microscopy (HAADF-STEM) image: (**a**) and particle size distribution (**b**) of the SnO_2 matrix.
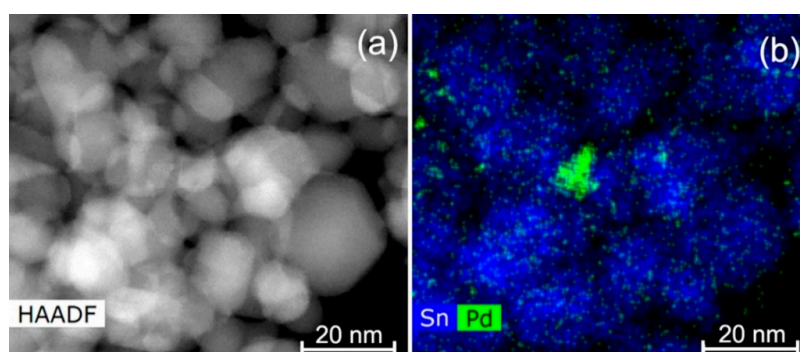
Figure 5. HAADF-STEM image: (**a**) energy dispersive X-ray scanning transmission electron microscopy (EDX-STEM) map (**b**) of the SnO_2/Pd nanocomposite.
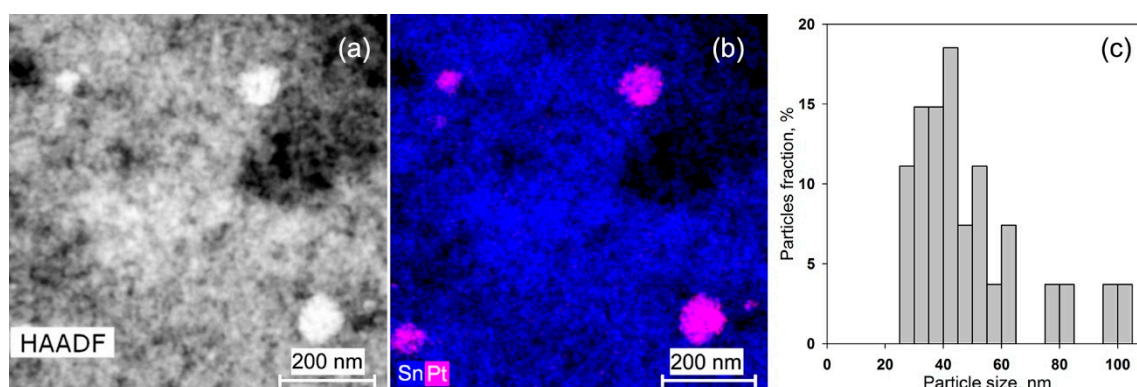
Figure 6. HAADF-STEM image: (**a**) EDX-STEM map (**b**) and Pt particles size distribution (**c**) of the SnO_2/Pt nanocomposite.
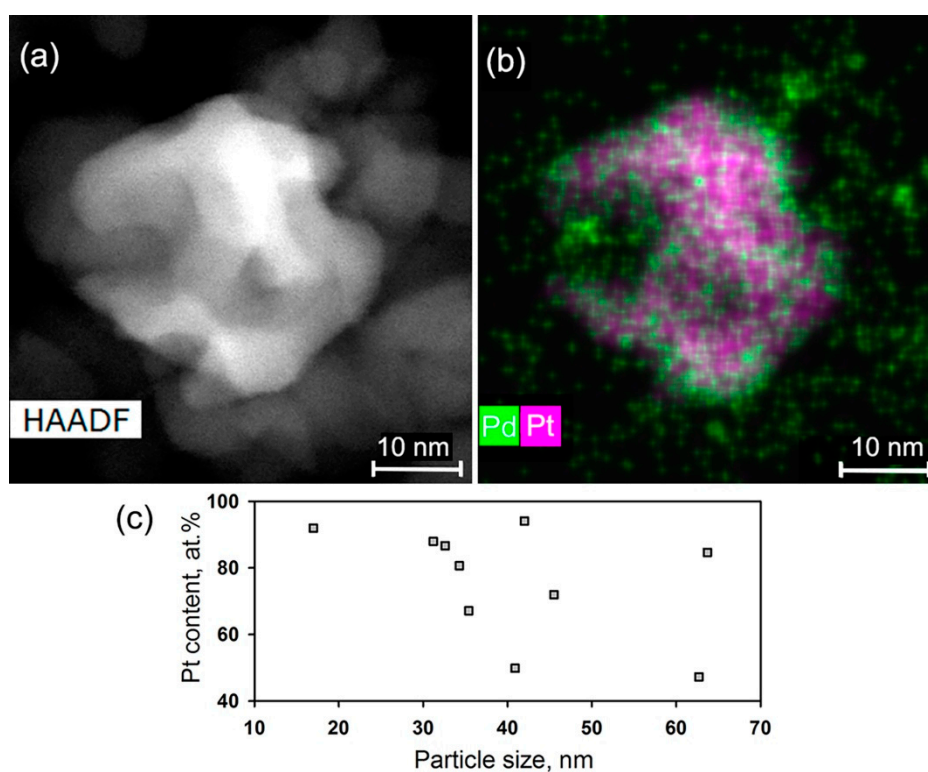
Figure 7. HAADF-STEM image: (**a**) EDX-STEM map (**b**) of the SnO_2/PtPd nanocomposite. (**c**) Pt content in PtPd nanoparticles of different size.

The Pd3d and Pt4f X-ray photoelectron spectroscopy (XPS) signals of the nanocomposites SnO_2/Pd, SnO_2/Pt, and SnO_2/PtPd could be fitted by only one doublet component (Figure 8a,b). Table 2 presents the Pd $3d_{5/2}$ and Pt $4f_{7/2}$ XPS spectral assignments. When comparing the estimated Pd $3d_{5/2}$ binding energies with reference data [65], we concluded that in SnO_2/Pd nanocomposite, palladium was present in the +2 oxidation state corresponding to the PdO. The Pd3d XP spectrum of the nanocomposite SnO_2/PtPd was shifted toward lower energies (Figure 8a), indicating a partial reduction of Pd. However, it was not possible to decompose the spectrum into two components that corresponded to different palladium oxidation states (0, +2). The Pt4f XP spectra of both SnO_2/Pt and SnO_2/PtPd nanocomposites corresponded to the Pt + 2 oxidation state in PtO [66]. When taking into account how the depth of the XPS analysis was determined by the mean free path of electrons with respect to inelastic collisions, and is 0.5–2.5 nm for metals and 4–10 nm for organic substances, it was impossible to exclude the presence of Pd^0 and especially, Pt^0 inside the particles (under the oxide layer).

The O1s XP spectra consisted of two components (Figure 8c) corresponding to the oxygen anions in the SnO_2 lattice (530.7–530.9 eV) and to different forms of chemisorbed oxygen and hydroxyl groups on the SnO_2 surface (531.8–532.0 eV). The impact of the higher energy component is 23–27% and did not depend significantly on the type of modifier.

Table 2. Pd $3d_{5/2}$ and Pt $4f_{7/2}$ XP spectral assignments.

Spectral Assignment	Binding Energy, eV				
	Ref. [65]	Ref. [66]	SnO_2/Pd	SnO_2/Pt	SnO_2/PtPd
Pd $3d_{5/2}$	Pd (0) 335.4 PdO 336.4		336.9	-	336.0
Pt $4f_{7/2}$		Pt (0) 71.0 Pt (II) 72.4 Pt (IV) 74.9	-	72.0	72.2
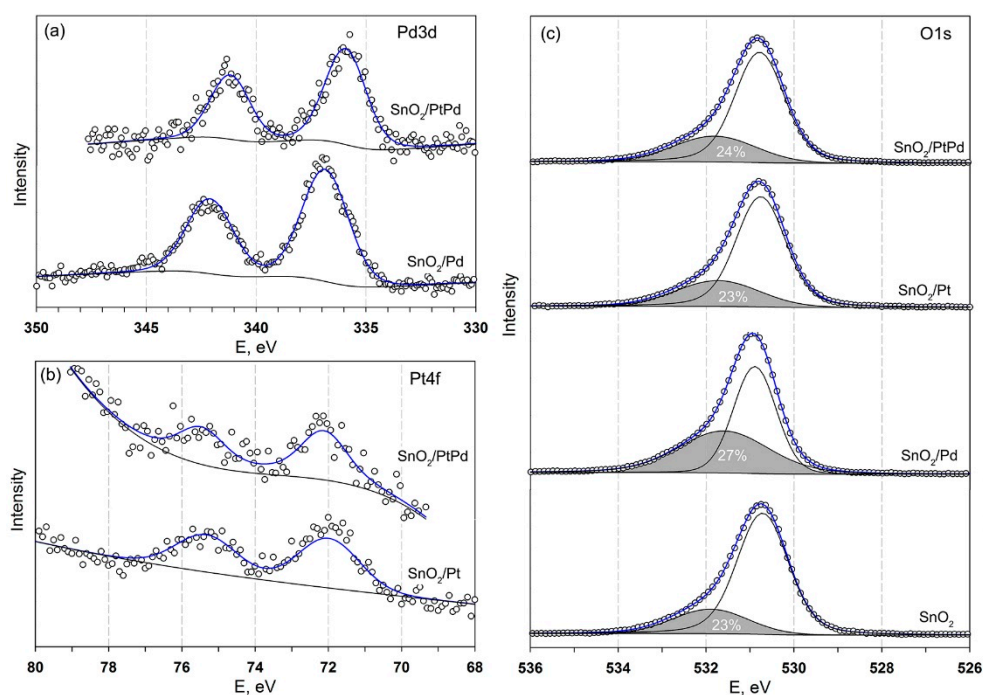
Figure 8. XP spectra Pd3d, (**a**) Pt4f, (**b**) O1s (**c**) of the samples.

The infra red (IR) spectra of blank SnO_2 samples and nanocomposites are compared in Figure 9a. The intense absorption band at 400–800 cm^{-1} corresponded to the oscillations of Sn-O-Sn bridges (670 cm^{-1}), Sn-OH terminal bonds (590 cm^{-1}), and surface (540 cm^{-1}) and bulk (480–460 cm^{-1}) phonon vibrations of SnO_2 [67]. The other absorption bands in the spectrum, apparently, were due to adsorbates. For a clear comparison of their concentration, the baselines were subtracted from the spectra, and the transmission in the whole range was normalized to the peak of the lattice vibrations at 670 cm^{-1}. The broad absorption band at 3300–3650 cm^{-1}, apparently referred to the stretching vibrations of O-H adsorbed water derivatives [68]. The modification of tin dioxide with palladium led to a significant increase in the concentration of surface hydroxyl groups, as evidenced by the increase in absorption in the range of 3300–3650 cm^{-1}. On the contrary, the introduction of platinum did not have any effect on the concentration of hydroxyl groups on the SnO_2 surface. For the SnO_2/PtPd nanocomposite, a nonadditive increase in the concentration of OH groups was observed in comparison with SnO_2/Pt and SnO_2/Pd nanocomposites.

(**a**)　　　　　　　　　　　　　　　　　(**b**)
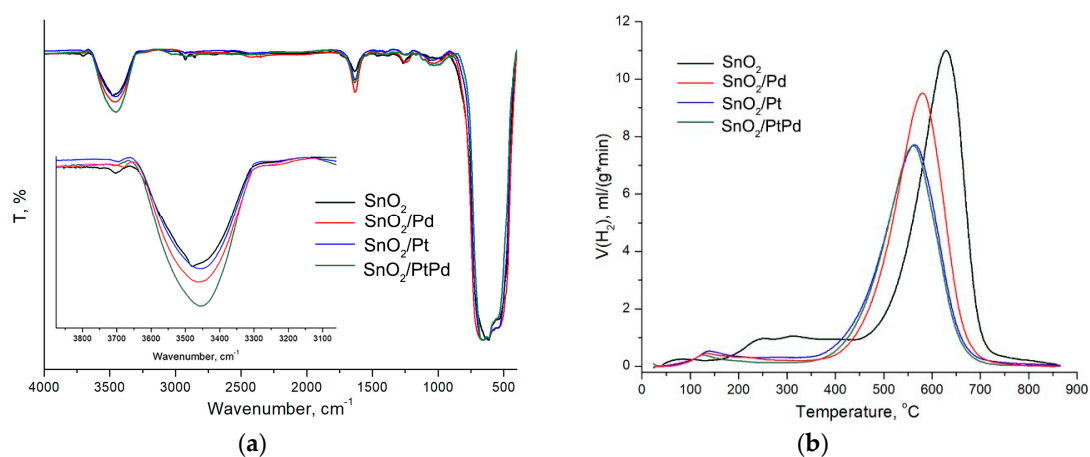
Figure 9. (**a**) IR spectra of blank SnO_2 and nanocomposites normalized to the intensity Sn-O oscillations. Inset: enlarged spectra in 3100–3800 cm^{-1} region. (**b**) TPR-H_2 profiles of blank SnO_2 and nanocomposites.

The results of the TPR-H$_2$ experiments are shown in Figure 9b and in Table 3. The high-temperature (350–850 °C) peak corresponded to the hydrogen consumption because of SnO$_2$ reduction to metallic tin:

$$SnO_2 + 2H_2 = Sn + 2H_2O \tag{2}$$

For nanocomposites SnO$_2$/Pd, SnO$_2$/Pt, and SnO$_2$/PtPd, a shift was observed from the high-temperature maximum of hydrogen consumption to the lower temperature region. This may be due to the catalytic activity of noble metal clusters in the matrix of nanocrystalline tin dioxide. The most probable mechanism was the hydrogen and oxygen joint spillover [69] of the SnO$_2$ crystal lattice through the clusters of modifiers. The reduction of SnO$_2$ at a lower temperature became possible due to the dissociation of hydrogen molecules on noble metal clusters. Examples illustrating such a mechanism of interaction with the gas phase for different "noble metal/metal oxide" systems were provided in the review [69]. By the oxygen isotopic exchange method [70], it was established that the modification of nanocrystalline tin dioxide with palladium and ruthenium resulted in the realization of a multistage heteroexchange mechanism, involving the dissociation of the O$_2$ molecule on the surface of the clusters of platinum-group metals, spillover of atomic oxygen from the clusters of modifiers to the SnO$_2$ surface, and its rapid exchange with the oxygen of the crystal lattice of tin dioxide. According to the analysis of the oxygen isotopic exchange data presented in the review [71], platinum was more active in this process than palladium, explaining the more significant decrease in the temperature of the complete reduction of the SnO$_2$/Pt and SnO$_2$/PtPd nanocomposites compared to SnO$_2$/Pd.

The processes responsible for the H$_2$ consumption in low temperature region 100–300 °C can be expressed as follows

$$O^-_{2(ads)} + 2H_2 = 2H_2O + e^- \tag{3}$$

$$O^-_{(ads)} + H_2 = H_2O + e^- \tag{4}$$

$$OH_{(ads)} + \frac{1}{2}H_2 = H_2O \tag{5}$$

The amount of oxygen adsorbed on the surface of SnO$_2$, estimated from TPR data under the assumption of interaction (3) is ~10^{-4} mol/m^2. Assuming an orientation along the normal to the surface and a radius as in the O$^-$ (1.76 Å) ion, the coverage of SnO$_2$ surface with hypothetical O$^-_{2(ads)}$ ions can be estimated at 0.5–1 monolayer. This is 2–3 orders of magnitude greater than the Weisz limitation for coverage of a semiconductor with charged adsorbates (10^{-2}–10^{-3} monolayer [72]), indicating that the real composition of oxidative adsorbates on the surface of materials was much more diverse than this assumption.

Modification of the SnO$_2$ surface with mono- and bimetallic clusters led to a decrease in the amount of hydrogen consumed in the low-temperature range. This indirectly indicated an increase in the fraction of the monatomic form of chemisorbed oxygen. Indeed, when comparing the reactions (3) and (4) surfaces with the same negative charge, predetermined by the Weitz limitation, it can be concluded that in the latter case, a smaller hydrogen consumption should be observed. In the case of nanocomposites containing palladium, the decrease in hydrogen absorption may be due to an increase in the concentration of hydroxyl groups detected by the IR spectroscopy and consequently, an increase in the contribution of the process (5).

Table 3. Results of the TPR-H$_2$ experiments.

| Sample	Hydrogen Consumption, Mol H$_2$ per 1 Mol SnO$_2$			T$_{max}$, °C	N (O$^-_{2(ads)}$), Mol/m^2
	Total	100–300 °C	370–850 °C		
SnO$_2$	2.9 ± 0.3	0.7 ± 0.1	2.2 ± 0.5	630	1.0×10^{-4}
SnO$_2$/Pd	2.5 ± 0.3	0.2 ± 0.1	2.3 ± 0.5	580	3.0×10^{-5}
SnO$_2$/Pt	2.3 ± 0.3	0.4 ± 0.1	1.9 ± 0.5	565	6.0×10^{-5}
SnO$_2$/PtPd	2.1 ± 0.3	0.2 ± 0.1	1.9 ± 0.5	565	3.0×10^{-5}

The obtained information on the structure and surface composition of SnO_2 and nanocomposites SnO_2/Pd, SnO_2/Pt, and $SnO_2/PtPd$ allowed us to explain the differences in their sensor properties to CO in dry (RH = 0%) and humid (RH = 20%) air.

SnO_2/Pd nanocomposite

For the SnO_2/Pd nanocomposite, the observed sensor response to CO in dry air was not unexpected and can be described within the framework of the concepts of electronic and chemical sensitization [2,5,11].

(i) Direct oxidation of CO gas molecules on the surface of PdO_x clusters resulted in a partial reduction of the modifier, while the fraction of Pd^0 increases:

$$PdO_x + xCO_{(gas)} \rightarrow Pd + xCO_{2(gas)}. \tag{6}$$
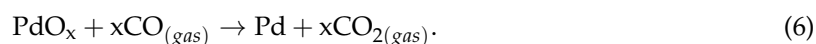
This effect corresponded to the mechanism of electronic sensitization. The electron work function φ for reduced palladium surface was smaller than in the case of PdO_x and is φ = 4.8 eV [73], which was close to the work function for SnO_2 (φ = 4.9 eV, [74]). Thus, as a result of the reduction of PdO_x clusters, a barrier was removed at the Pd/SnO_2 interface, which led to a decrease in material resistance and the sensor response appearance.

(ii) Strong chemisorption of CO molecules on Pd^0 was accompanied by a weakening of the intramolecular bond in CO and facilitated its break and further transformations of chemisorbed molecules:

$$Pd^0 + CO_{(gas)} \rightarrow Pd^{\delta+} - CO^{\delta-}. \tag{7}$$
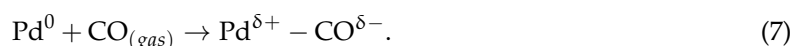
(iii) Modification with PdO_x clusters led to an increase in the SnO_2 concentration of paramagnetic centers ·OH and rooted hydroxyl groups OH···OH that participated in the low temperature oxidation of chemisorbed CO molecules:

$$CO_{(gas)} + OH_{surf} \rightarrow CO_{2(gas)} + H^+ + e^-. \tag{8}$$
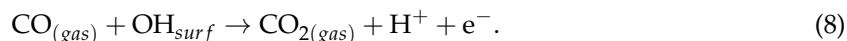
The increase in humidity led to a decrease in the sensitivity of SnO_2/Pd in the low temperature region due to competitive adsorption of water molecules and blocking of active sites on the surface of SnO_2 and PdO_x clusters [75].

SnO_2/Pt nanocomposite

The low response of nanocomposites SnO_2/Pt was caused by direct CO oxidation on PtO_x clusters. Based on the results of complementary investigations by in situ and *operando* X-ray absorption spectroscopy and *operando* FT-IR spectroscopy, D. Degler et al. found that CO oxidation mainly occurs at the PtO_x surface (Pt–*O*–Pt sites) [76]. This led to a decrease in the quantity of CO molecules that can react with the oxygen chemisorbed on SnO_2 surface. The authors assumed that if platinum is introduced by impregnation after the calcination of the SnO_2 matrix, it forms a separate oxide phase, which creates additional reaction sites not electronically coupled to the SnO_2. In our investigation, this assumption could not be used since the introduction of PtO_x clusters led to the important ($\sim10^3$ times) increase in SnO_2 resistance in dry air (Figure 1a). The work function of metallic Pt was sufficiently high (φ = 5.65 eV [77]). Covering platinum with a full monolayer of oxygen led to the further increase in the work function by 1.19 eV (φ ~6.8 eV) [78]. When a contact was formed between PtO_x nanoparticles and SnO_2 (φ = 4.9 eV), the Fermi level of the semiconductor oxide was pinned to the Pt^{2+}/Pt^0 potential. This led to the formation of an electron depleted space charge region and to an increase in the SnO_2 resistivity. As in the case of PdO_x, it was possible that PtO_x clusters reduced upon interaction with CO [79]. However, the work function of metallic Pt significantly exceeded the corresponding value for SnO_2. As a result, the band-bending at the Pt/SnO_2 interface persisted in the presence of CO, which led to a low sensor response of SnO_2/Pt nanocomposite when CO was detected in dry air.

In humid air, the Pt–*O*–Pt sites were deactivated [76] because of strong water adsorption on PtO$_x$ clusters [75]. This should have led to a decrease in the amount of CO oxidized directly on the clusters of the modifier, and consequently, to an increase in the sensor response due to an increase in the amount of CO oxidized by oxygen chemisorbed on the SnO$_2$ surface. However, in humid air, the surface of tin dioxide also became inactive due to the partial replacement of chemisorbed oxygen by hydroxyl groups according to the following reaction [80]

$$H_2O_{(gas)} + 2 \cdot Sn_{Sn} + O^{\alpha-}_{(ads)} \rightarrow 2 \cdot (Sn - OH) + \alpha \cdot e^- \tag{9}$$
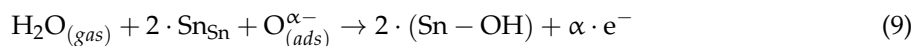
The combination of these factors suggests that CO oxidation can take place at the Pt–*O*–Sn sites at the three-phase boundary between PtO$_x$ and SnO$_2$ [76], providing a very slight increase in sensor response as compared with detection in dry air.

SnO$_2$/PtPd nanocomposite

A feature of the SnO$_2$/PtPd nanocomposite was a two-level distribution of the modifiers over the surface of the semiconductor matrix: platinum only existed as a part of large (20–60 nm) bimetallic particles PtPdO$_x$ with a Pt content generally exceeding 50 mol%, while palladium was distributed between these large bimetallic particles PtPdO$_x$ and small (~2 nm) particles PdO$_x$. As a result of this distribution of modifiers, the active sites on the surface of SnO$_2$/PtPd were a combination of the centers characteristic for SnO$_2$/Pt and SnO$_2$/Pd. Thus, the temperature of SnO$_2$ reduction in the SnO$_2$/PtPd nanocomposite coincided with that of SnO$_2$/Pt (Figure 9b), which was due to the presence of particles enriched in platinum. At the same time, an increase in the concentration of hydroxyl groups on the surface of SnO$_2$/PtPd (Figure 9a) was determined by the presence of small PdO$_x$ particles.

However, when comparing the sensor response, such an additive picture was not observed. To explain the inversion of sensor response from *n*- to *p*-type observed in dry conditions, it was necessary to analyze the combined effect of the modifiers on the electrophysical properties of SnO$_2$. Since metals Pt, Pd, and, to a greater extent, their oxides, are characterized by a higher work function than SnO$_2$, in the contact areas SnO$_2$-PtPdO$_x$ and SnO$_2$-PdO$_x$, an electron-depleted layer formed in SnO$_2$. The depth of this layer was determined using the height of the energy barrier—i.e., the difference in the work function values of the contacting materials—and the lateral length along the surface was determined by the area of the contact between SnO$_2$ and clusters of modifiers. In the SnO$_2$/PtPd nanocomposite, bimetallic particles enriched in platinum form on the surface of the SnO$_2$ agglomerates regions with a deep depleted layer, while small PdO$_x$ particles formed extended space charge regions of the surface of SnO$_2$ grains. As a result, it can be expected that the concentration of electrons in SnO$_2$ near the surface layer became so low that they ceased to be the main charge carriers. Such a change in the response type was reported for various oxides: from *n*- to *p*-type for MoO$_3$ [81], In$_2$O$_3$ [82], SnO$_2$(Fe) [83], ZnO [84], WO$_3$ [85], WO$_3$ nanorods [86], TiO$_2$ nanofibers [87], and from *p*- to *n*-type conductivity for α-Fe$_2$O$_3$ [88]. The inversion of the sensor response was explained by a change in the type of main charge carriers in semiconductor oxide due to either the surface reactions under certain conditions, or because of the effect of impurities.

In dry air, in the high temperature region, the *p*-type response of the SnO$_2$/PtPd nanocomposite had a similar temperature dependence as the *n*-type response of the SnO$_2$/Pd nanocomposite. It indicated that under these conditions, the PdO$_x$ small nanoparticles determined the reactivity of SnO$_2$/PtPd sample through reaction (6). The reduced amplitude of the *p*-type response of SnO$_2$/PtPd nanocomposite compared with the *n*-type response of SnO$_2$/Pd was because of the direct oxidation of part of the CO molecules on the surface of large bimetallic PtPdO$_x$ particles. This process did not alter the concentration of charge carriers in the SnO$_2$ semiconductor matrix.

In humid air, the adsorption of water vapor on SnO$_2$, in addition to blocking the active centers, led to an increase in the concentration of electrons and in the conductivity of SnO$_2$ (reaction (9)). Comparison of the data presented in Figure 1a,b, clearly demonstrates that an increase in the air relative humidity (25 °C) from RH = 0% to RH = 20% reduced the resistance of all samples by about

10 times at each measurement temperature. Thus, in a humid atmosphere, electrons remained the main charge carriers in the SnO_2/PtPd nanocomposite and no inversion of sensor response from *n*- to *p*-type was observed.

3. Materials and Methods

The synthesis of nanocrystalline SnO_2 was carried out using flame spray pyrolysis (FSP). First, 20 mL of tin (II) 2-ethylhexanoate was dissolved in 60 mL of toluene; the resulting solution was divided into four equal parts, each of them then slowly injected into the FSP reactor. After the completion of each injection, the apparatus was dismantled, tin dioxide powder was collected, and a clean filter was installed. The obtained portions of the powder were combined and annealed in air at 400 °C for 24 h.

For the modification by impregnation method, the solutions of Pt (II) acetylacetonate and Pd (II) acetylacetonate in ethanol were used as metal precursors. The calculated volume of the precursor solution was added to the weighed SnO_2 powder to obtain 1 wt.% total metal content (1 wt.% M for monometallic nanocomposites and 0.5 wt.% Pd + 0.5 wt.% Pt for bimetallic one) and ethanol was allowed to evaporate. All impregnated samples were then annealed at 300 °C for 24 h for decomposition of acetylacetonates. These annealing conditions corresponded to the lowest temperature, which ensured complete decomposition of both $Pd(acac)_2$ and $Pt(acac)_2$ that was proven using thermal analysis. A reference sample of SnO_2 was created using an annealing undoped matrix material at 300 °C for 24 h.

The elemental composition of mono- and bimetallic nanocomposites was determined by X-ray fluorescence (XRF) analysis using a M1 Mistral (Bruker) micro-X-ray spectrometer. The phase composition of the samples was determined by XRD using a DRON-4-07 diffractometer (CuK_α, $\lambda = 1.5406$ Å). The crystallite size of SnO_2 phase (d_{XRD}) was calculated by the Sherrer formula using 110 and 101 reflections.

The specific surface area was measured on Chemisorb 2750 instrument (Micromeritics) using a low-temperature nitrogen adsorption using single point BET model.

The microstructure of the samples and distribution of modifiers in SnO_2 matrix were investigated using transmission electron microscopy (TEM), high angle annular dark field scanning transmission electron microscopy (HAADF-STEM), and energy dispersive X-ray (EDX) mapping, all accomplished using a FEI Osiris microscope equipped with a Super-X detector operated at 200 kV.

The chemical state of the elements was studied by X-ray photoelectron spectroscopy (XPS). The measurements were effectuated on K-Alpha (Thermo Scientific) spectrometer equipped with a monochromatic Al K_α X-ray source (E = 1486.7 eV). The positions of the peaks in the binding energy scale were adjusted with a C1s peak (285.0 eV) that corresponded to the carbon contamination of the surface with an accuracy of 0.1 eV. XP-spectra were fitted by Gaussian–Lorentzian convolution functions with simultaneous optimization of the background parameters.

Active surface sites with oxidizing properties were investigated using the thermo-programmed reduction with hydrogen (TPR-H_2) method. The experiments were carried out on Chemisorb 2750 (Micromeritics) in a quartz reactor at a gas mixture flow of 10% H_2 in argon at 50 mL/min and at a heating rate of 10 °C/min to 900 °C.

The molecules adsorbed on the surface of materials were studied using the Fourier Transform infrared spectroscopy (FTIR) method. The IR spectra of the samples were taken on a Spectrum One (Perkin Elmer) spectrometer in transmission mode within the wavenumber range 400–4000 cm^{-1} with 1 cm^{-1} steps. The powders (5 mg) were grinded with 100 mg of dried KBr (Aldrich, "for FTIR analysis") and pressed into tablets.

To perform the sensor tests, the powders were deposited onto microelectronic transducers equipped with Pt contacts and heaters in form of thick films. The sensors were placed into a gas flow chamber under conditions of a controlled gas flow of 100 ± 0.1 mL/min and operated by a resistance-measuring device connected to a PC. The DC-resistance was registered in situ under changing conditions in a temperature range of 60–300 °C. CO-air mixture containing 6.7 ppm CO was

used as a test gas. The required level of humidity (RH = 0% and RH = 20%) was provided by mixing two streams of dry air and humid air using the membrane humidifier Cellkraft P-2.

4. Conclusions

The nanocrystalline SnO_2 was synthesized using flame spray pyrolysis and used as semiconductor matrix to obtain the mono- and bimetallic nanocomposites SnO_2/Pd, SnO_2/Pt and $SnO_2/PtPd$. It was found that in monometallic nanocomposites SnO_2/Pt and SnO_2/Pd, platinum forms large (several tens of nanometers) particles, PtO_x, while palladium was distributed as small (including less than 2 nm) PdO_x nanoparticles on the SnO_2 surface. In bimetallic nanocomposite $SnO_2/PtPd$, platinum was located in large bimetallic PtPdOx particles with a different Pt/Pd ratio, but palladium was also present in the form of small nanoparticles PdO_x.

The surface characteristics of bimetallic $SnO_2/PtPd$ nanocomposite were not additive as compared with monometallic SnO_2/Pt and SnO_2/Pd samples. Thus, active surface sites with oxidizing properties were determined by the presence of Pt-containing particles, while PdO_x nanoparticles were responsible for the increase in the surface hydroxyl concentration.

The sensor properties of bimetallic $SnO_2/PtPd$ nanocomposite can be explained by the combined effect of modifiers on the electrophysical properties of SnO_2. The inversion of the sensor response from *n*- to *p*-type observed for $SnO_2/PtPd$ nanocomposite in dry air was due to a change in the type of main charge carriers in the near-surface layer of SnO_2. Furthermore, the chances was due to the formation of a deep and extended electron depleted layer in the area of SnO_2 contacts with platinum-enriched bimetallic $PtPdO_x$ particles and PdO_x nanoparticles. In humid air, the adsorption of water vapor on SnO_2 led to an increase in the concentration of electrons. As a result, electrons remained the main charge carriers and no inversion of sensor response was observed.

References

1. Das, S.; Jayaraman, V. SnO₂: A comprehensive review on structure and gas sensors. *Prog. Mater. Sci.* **2014**, *66*, 112–255. [CrossRef]
2. Gurlo, A.; Bârsan, N.; Weimar, U. Gas Sensors Based on Semiconducting Metal Oxides. In *Metal Oxides. Chemistry and Applications*; Fierro, J.L.G., Ed.; CRC Press, Taylor & Francis Group: Boca Raton, FL, USA, 2006; pp. 683–738, ISBN 978-0-8247-2371-2.
3. Krivetskiy, V.V.; Rumyantseva, M.N.; Gaskov, A.M. Chemical modification of nanocrystalline tin dioxide for selective gas sensors. *Russ. Chem. Rev.* **2013**, *82*, 917–941. [CrossRef]
4. Korotcenkov, G.; Cho, B.K. Metal oxide composites in conductometric gas sensors: Achievements and challenges. *Sens. Actuators B* **2017**, *244*, 182–210. [CrossRef]
5. Marikutsa, A.V.; Vorobyeva, N.A.; Rumyantseva, M.N.; Gaskov, A.M. Active sites on the surface of nanocrystalline semiconductor oxides ZnO and SnO₂ and gas sensitivity. *Russ. Chem. Bull.* **2017**, *66*, 1728–1764. [CrossRef]
6. Zhou, X.; Lee, S.; Xu, Z.; Yoon, J. Recent Progress on the Development of Chemosensors for Gases. *Chem. Rev.* **2015**, *115*, 7944–8000. [CrossRef] [PubMed]
7. WHO. *Air Quality Guidelines for Europe*, 2nd ed.; WHO: Geneva, Switzerland, 2000; Available online: http://www.euro.who.int/__data/assets/pdf_file/0020/123059/AQG2ndEd_5_5carbonmonoxide.PDF?ua=1 (accessed on 29 August 2018).

8. Eranna, G.; Joshi, B.C.; Runthala, D.P.; Gupta, R.P. Oxide materials for development of integrated gas sensors—A comprehensive review. *Crit. Rev. Solid State Mater. Sci.* **2004**, *29*, 111–188. [CrossRef]

9. Savchenko, V.I. The Chemisorption of Oxygen and the Oxidation of Carbon Monoxide on Metals. *Russ. Chem. Rev.* **1986**, *55*, 222–231. [CrossRef]

10. Over, H.; Muhler, M. Catalytic CO oxidation over ruthenium—Bridging the pressure gap. *Prog. Surf. Sci.* **2003**, *72*, 3–17. [CrossRef]

11. Yamazoe, N.; Kurokawa, Y.; Seiyama, T. Effects of additives on semiconductor gas sensors. *Sens. Actuators B* **1983**, *4*, 283–289. [CrossRef]

12. Rella, R.; Siciliano, P.; Capone, S.; Epifani, M.; Vasanelli, L.; Licciulli, A. Air quality monitoring by means of sol–gel integrated tin oxide thin films. *Sens. Actuators B* **1999**, *58*, 283–288. [CrossRef]

13. Cabot, A.; Arbiol, A.; Morante, J.R.; Weimar, U.; Bârsan, N.; Göpel, W. Analysis of the noble metal catalytic additives introduced by impregnation of as obtained SnO sol–gel nanocrystals for gas sensors. *Sens. Actuators B* **2000**, *70*, 87–100. [CrossRef]

14. Korotcenkov, G.; Brinzari, V.; Boris, Y.; Ivanov, M.; Schwank, J.; Morante, J. Influence of surface Pd doping on gas sensing characteristics of SnO_2 thin films deposited by spray pyrolysis. *Thin Solid Films* **2003**, *436*, 119–126. [CrossRef]

15. Ramgir, N.S.; Hwang, Y.K.; Jhung, S.H.; Mulla, I.S.; Chang, J.-S. Effect of Pt concentration on the physicochemical properties and CO sensing activity of mesostructured SnO_2. *Sens. Actuators B* **2006**, *114*, 275–282. [CrossRef]

16. Belmonte, J.C.; Manzano, J.; Arbiol, J.; Cirera, A.; Puigcorbe, J.; Vila, A.; Sabate, N.; Gracia, I.; Cane, C.; Morante, J.R. Micromachined twin gas sensor for CO and O_2 quantification based on catalytically modified nano-SnO_2. *Sens. Actuators B* **2006**, *114*, 881–892. [CrossRef]

17. Mädler, L.; Roessler, A.; Pratsinis, S.E.; Sahm, T.; Gurlo, A.; Barsan, N.; Weimar, U. Direct formation of highly porous gas-sensing films by in situ thermophoretic deposition of flame-made Pt/SnO_2 nanoparticles. *Sens. Actuators B* **2006**, *114*, 283–295. [CrossRef]

18. Koziej, D.; Barsan, N.; Shimanoe, K.; Yamazoe, N.; Szuber, J.; Weimar, U. Spectroscopic insights into CO sensing of undoped and palladium doped tin dioxide sensors derived from hydrothermally treated tin oxide sol. *Sens. Actuators B* **2006**, *118*, 98–104. [CrossRef]

19. Dolbec, R.; El Khakania, M.A. Sub-ppm sensitivity towards carbon monoxide by means of pulsed laser deposited SnO_2:Pt based sensors. *Appl. Phys. Lett.* **2007**, *90*, 173114. [CrossRef]

20. Lee, Y.C.; Huang, H.; Tan, O.K.; Tse, M.S. Semiconductor gas sensor based on Pd-doped SnO_2 nanorod thin films. *Sens. Actuators B* **2008**, *132*, 239–242. [CrossRef]

21. Huang, H.; Ong, C.Y.; Guo, J.; White, T.; Tse, M.S.; Tan, O.K. Pt surface modification of SnO_2 nanorod arrays for CO and H_2 sensors. *Nanoscale* **2010**, *2*, 1203–1207. [CrossRef] [PubMed]

22. Marikutsa, A.V.; Rumyantseva, M.N.; Yashina, L.V.; Gaskov, A.M. Role of surface hydroxyl groups in promoting room temperature CO sensing by Pd-modified nanocrystalline SnO_2. *J. Solid State Chem.* **2010**, *183*, 2389–2399. [CrossRef]

23. Wang, K.; Zhao, T.; Lian, G.; Yu, Q.; Luan, C.; Wang, Q.; Cui, D. Room temperature CO sensor fabricated from Pt-loaded SnO_2 porous nanosolid. *Sens. Actuators B* **2013**, *184*, 33–39. [CrossRef]

24. Zhukova, A.A.; Rumyantseva, M.N.; Zaytsev, V.B.; Zaytseva, A.V.; Abakumov, A.M.; Gaskov, A.M. Pd nanoparticles on SnO_2(Sb) whiskers: Aggregation and reactivity in CO detection. *J. Alloys Compd.* **2013**, *565*, 6–10. [CrossRef]

25. Marikutsa, A.V.; Rumyantseva, M.N.; Gaskov, A.M. Specific interaction of PdO_x- and RuO_y-modified tin dioxide with CO and NH_3 gases: Kelvin probe and drift studies. *J. Phys. Chem. C* **2015**, *119*, 24342–24350. [CrossRef]

26. Wang, Q.; Wang, C.; Sun, H.; Sun, P.; Wang, Y.; Lin, J.; Lu, G. Microwave assisted synthesis of hierarchical Pd/SnO_2 nanostructuresfor CO gas sensor. *Sens. Actuators B* **2016**, *222*, 257–263. [CrossRef]

27. Wang, Q.; Li, X.; Liu, F.; Liu, C.; Su, T.; Lin, J.; Sun, P.; Sun, Y.; Liu, F.; Lu, G. The enhanced CO gas sensing performance of Pd/SnO_2 hollow sphere sensors under hydrothermal conditions. *RSC Adv.* **2016**, *6*, 80455–80461. [CrossRef]

28. Guczi, L. Bimetallic nano-particles: Featuring structure and reactivity. *Catal. Today* **2005**, *101*, 53–64. [CrossRef]

29. Rodriguez, J.A. Electronic and chemical properties of Pt, Pd and Ni in bimetallic surfaces. *Surf. Sci.* **1996**, *345*, 347–362. [CrossRef]

30. Wang, H.; Yang, W.; Tian, P.; Zhou, J.; Tang, R.; Wu, S. A highly active and anti-coking Pd-Pt/SiO$_2$ catalyst for catalytic combustion of toluene at low temperature. *Appl. Catal. A* **2017**, *529*, 60–67. [CrossRef]

31. Calzada, L.A.; Collins, S.E.; Han, C.W.; Ortalan, V.; Zanella, R. Synergetic effect of bimetallic Au-Ru/TiO$_2$ catalysts for complete oxidation of methanol. *Appl. Catal. B* **2017**, *207*, 79–92. [CrossRef]

32. Toshima, N.; Kushihashi, K.; Yonezawa, T.; Hirai, H. Colloidal Dispersions of Palladium–Platinum Bimetallic Clusters Protected by Polymers. Preparation and Application to Catalysis. *Chem. Lett.* **1989**, *18*, 1769–1772. [CrossRef]

33. Toshima, N.; Yonezawa, T.; Kushihashi, K. Polymer-protected palladium–platinum bimetallic clusters: Preparation, catalytic properties and structural considerations. *J. Chem. Soc. Faraday Trans.* **1993**, *89*, 2537–2543. [CrossRef]

34. Cho, S.J.; Kang, S.K. Structural transformation of PdPt nanoparticles probed with X-ray absorption near edge structure. *Catal. Today* **2004**, *93*, 561–566. [CrossRef]

35. Endo, T.; Kuno, T.; Yoshimura, T.; Esumi, K. Preparation and Catalytic Activity of Au–Pd, Au–Pt, and Pt–Pd Binary Metal Dendrimer Nanocomposites. *J. Nanosci. Nanotechnol.* **2005**, *5*, 1875–1882. [CrossRef] [PubMed]

36. Jin, X.; Zhao, M.; Vora, M.; Shen, J.; Zeng, C.; Yan, W.; Thapa, P.S.; Subramaniam, B.; Chaudhari, R.V. Synergistic Effects of Bimetallic PtPd/TiO$_2$ Nanocatalysts in Oxidation of Glucose to Glucaric Acid: Structure Dependent Activity and Selectivity. *Ind. Eng. Chem. Res.* **2016**, *55*, 2932–2945. [CrossRef]

37. Ma, L.; Zhou, L.; He, Y.; Wang, L.; Huang, Z.; Jiang, Y.; Gao, J. Mesoporous Bimetallic PtPd Nanoflowers as a Platform to Enhance Electrocatalytic Activity of Acetylcholinesterase for Organophosphate Pesticide Detection. *Elecroanalysis* **2018**, *30*, 1801–1810. [CrossRef]

38. Zhang, J.; Gan, W.; Fu, X.; Hao, H. A microwave assisted one-pot route synthesis of bimetallic PtPd alloy cubic nanocomposites and their catalytic reduction for 4-nitrophenol. *Mater. Res. Express* **2017**, *4*, 105022. [CrossRef]

39. Navarro, R.M.; Pawelec, V.; Trejo, J.M.; Mariscal, R.; Fierro, J.L.G. Hydrogenation of Aromatics on Sulfur-Resistant PtPd Bimetallic Catalysts. *J. Catal.* **2000**, *189*, 184–194. [CrossRef]

40. Xia, T.; Shen, H.; Chang, G.; Zhang, Y.; Shu, H.; Oyama, M.; He, Y. Facile and Rapid Synthesis of Ultrafine PtPd Bimetallic Nanoparticles and Their High Performance toward Methanol Electrooxidation. *J. Nanomater.* **2014**, *2014*, 496249. [CrossRef]

41. Korotcenkov, G. *Handbook of Gas Sensor Materials. Properties, Advantages and Shortcomungs for Applications. Vol. 1. Convenional Approaches*; Springer Science +Business Media, LLC: New York, NY, USA, 2013; pp. 279–281, ISBN 978-1-4614-7164-6.

42. Zhang, T.; Liu, L.; Qi, Q.; Li, S.; Lu, G. Development of microstructure In/Pd-doped SnO$_2$ sensor for low-level CO detection. *Sens. Actuators B* **2009**, *139*, 287–291. [CrossRef]

43. Yin, X.-T.; Guo, X.-M. Selectivity and sensitivity of Pd-loaded and Fe-doped SnO$_2$ sensor for CO detection. *Sens. Actuators B* **2014**, *200*, 213–218. [CrossRef]

44. Mutinati, G.C.; Brunet, E.; Koeck, A.; Steinhauer, S.; Yurchenko, O.; Laubender, E.; Urban, G.; Siegert, J.; Rohracher, K.; Schrank, F.; et al. Optimization of CMOS integrated nanocrystalline SnO$_2$ gas sensor devices with bimetallic nanoparticles. *Procedia Eng.* **2014**, *87*, 787–790. [CrossRef]

45. Kim, S.-J.; Choi, S.-J.; Jang, J.-S.; Cho, H.-J.; Koo, W.-T.; Tuller, H.L.; Kim, I.-D. Exceptional High-Performance of Pt-Based Bimetallic Catalysts for Exclusive Detection of Exhaled Biomarkers. *Adv. Mater.* **2017**, *29*, 1700737. [CrossRef] [PubMed]

46. Chaudhary, V.A.; Mulla, I.S.; Vijayamohanan, K. Synergetic sensitivity effects in surface modified tin oxide hydrogen sensors using ruthenium and palladium oxides. *J. Mater. Sci. Lett.* **1997**, *16*, 1819–1821. [CrossRef]

47. Chaudhary, V.A.; Mulla, I.S.; Vijayamohanan, K. Selective hydrogen sensing properties of surface functionalized tin oxide. *Sens. Actuators B* **1999**, *55*, 154–160. [CrossRef]

48. Choi, U.-S.; Sakai, G.; Shimanoe, K.; Yamazoe, N. Sensing properties of Au-loaded SnO$_2$–Co$_3$O$_4$ composites to CO and H$_2$. *Sens. Actuators B* **2005**, *107*, 397–401. [CrossRef]

49. Vladimirova, S.A.; Rumyantseva, M.N.; Filatova, D.G.; Kozlovskii, V.F.; Chizhov, A.S.; Khmelevskii, N.O.; Marchevskii, A.V.; Li, X.; Gaskov, V. SnO$_2$(Au^0, Co^{II,III}) Nanocomposites: A Synergistic Effect of the Modifiers in CO Detection. *Inorg. Mater.* **2016**, *52*, 94–100. [CrossRef]

50. Badalyan, S.M.; Rumyantseva, M.N.; Nikolaev, S.A.; Marikutsa, A.V.; Smirnov, V.V.; Alikhanian, A.S.; Gaskov, A.M. Effect of Au and NiO catalysts on the NO$_2$ sensing properties of nanocrystalline SnO$_2$. *Inorg. Mater.* **2010**, *46*, 232–236. [CrossRef]

51. Choi, S.-W.; Katoch, A.; Sun, G.-J.; Kim, S.S. Bimetallic Pd/Pt nanoparticle-functionalized SnO$_2$ nanowires for fast response and recovery to NO$_2$. *Sens. Actuators B* **2013**, *181*, 446–453. [CrossRef]

52. Malkov, I.V.; Krivetskiy, V.V.; Potemkin, D.I.; Zadesenets, A.V.; Batuk, M.M.; Hadermann, J.; Marikutsa, A.V.; Rumyantseva, M.N.; Gaskov, A.M. Effect of Bimetallic Pd/Pt Clusters on the Sensing Properties of Nanocrystalline SnO$_2$ in the Detection of CO. *Russ. J. Inorg. Chem.* **2018**, *63*, 1007–1011. [CrossRef]

53. Krivetskiy, V.; Ponzoni, A.; Comini, E.; Badalyan, S.; Rumyantseva, M.; Gaskov, A. Selectivity Modification of SnO$_2$-Based Materials for Gas Sensor Arrays. *Electroanalysis* **2010**, *22*, 2809–2816. [CrossRef]

54. Teoh, W.Y.; Amala, R.; Mädler, L. Flame spray pyrolysis: An enabling technology for nanoparticles design and fabrication. *Nanoscale* **2010**, *2*, 1324–1347. [CrossRef] [PubMed]

55. Kemmler, J.A.; Pokhrel, S.; Mädler, L.; Weimar, U.; Bârsan, N. Flame spray pyrolysis for sensing at the nanoscale. *Nanotechnology* **2013**, *24*, 442001. [CrossRef] [PubMed]

56. Koirala, R.; Pratsinisa, S.E.; Baiker, A. Synthesis of catalytic materials in flames: Opportunities and challenges. *Chem. Soc. Rev.* **2016**, *45*, 3053–3068. [CrossRef] [PubMed]

57. Inyawilert, K.; Wisitsoraat, A.; Tuantranont, A.; Phanichphant, S.; Liewhiran, C. Ultra-sensitive and highly selective H$_2$ sensors based on FSP-made Rh-substituted SnO$_2$ sensing films. *Sens. Actuators B* **2017**, *240*, 1141–1152. [CrossRef]

58. Li, Y.; Hu, Y.; Jiang, H.; Hou, X.; Li, C. Construction of core–shell Fe$_2$O$_3$@SnO$_2$ nanohybrids for gas sensors by a simple flame-assisted spray process. *RSC Adv.* **2013**, *3*, 22373–22379. [CrossRef]

59. Tricoli, A.; Graf, M.; Pratsinis, S.E. Optimal Doping for Enhanced SnO$_2$ Sensitivity and Thermal Stability. *Adv. Funct. Mater.* **2008**, *18*, 1969–1976. [CrossRef]

60. Liewhiran, C.; Tamaekong, N.; Wisitsoraat, A.; Phanichphant, S. H$_2$ Sensing Response of Flame-Spray-Made Ru/SnO$_2$ Thick Films Fabricated from Spin-Coated Nanoparticles. *Sensors* **2009**, *9*, 8996–9010. [CrossRef] [PubMed]

61. Liewhiran, C.; Tamaekong, N.; Wisitsoraat, A.; Phanichphant, S. The effect of Pt nanoparticles loading on H$_2$ sensing properties of flame-spray-made SnO$_2$ sensing films. *Mater. Chem. Phys.* **2014**, *147*, 661–672. [CrossRef]

62. Sukunta, J.; Wisitsoraat, A.; Tuantranont, A.; Phanichphant, S.; Liewhiran, C. Highly-sensitive H$_2$S sensors based on flame-made V-substituted SnO$_2$ sensing films. *Sens. Actuators B* **2017**, *242*, 1095–1107. [CrossRef]

63. Kotchasak, N.; Wisitsoraat, A.; Tuantranont, A.; Phanichphant, S.; Yordsri, V.; Liewhiran, C. Highly sensitive and selective detection of ethanol vapor using flame-spray-made CeO$_x$-doped SnO$_2$ nanoparticulate thick films. *Sens. Actuators B* **2018**, *255*, 8–21. [CrossRef]

64. Rebholz, J.; Jaeschke, C.; Hübner, M.; Pham, D.; Mädler, L.; Weimar, U.; Bârsan, N. Conduction Mechanism in Undoped and Antimony Doped SnO$_2$ Based FSP Gas Sensors. In Proceedings of the 14th International Meeting on Chemical Sensors, Nuremberg, Germany, 20–23 May 2012; pp. 105–108. [CrossRef]

65. XPS Interpretation of Palladium. Available online: https://xpssimplified.com/elements/palladium.php (accessed on 14 October 2018).

66. XPS Interpretation of Platinum. Available online: https://xpssimplified.com/elements/platinum.php (accessed on 14 October 2018).

67. Liu, Y.; Yang, F.; Yang, X. Size-controlled synthesis and characterization of quantum-size SnO$_2$ nanocrystallites by a solvothermal route. *Colloids Surf. A* **2008**, *312*, 219–225. [CrossRef]

68. Marikutsa, A.V.; Rumyantseva, M.N.; Konstantinova, E.A.; Shatalova, T.B.; Gaskov, A.M. Active sites on nanocrystalline tin dioxide surface: Effect of palladium and ruthenium oxides clusters. *J. Phys. Chem. C* **2014**, *118*, 21541–21549. [CrossRef]

69. Conner, W.C.; Falconer, J.L. Spillover in Heterogeneous Catalysis. *Chem. Rev.* **1995**, *95*, 759–788. [CrossRef]

70. Marikutsa, A.V.; Rumyantseva, M.N.; Frolov, D.D.; Morozov, I.V.; Boltalin, A.I.; Fedorova, A.A.; Petukhov, I.A.; Yashina, L.V.; Konstantinova, E.A.; Sadovskaya, V.; et al. Role of PdO$_x$ and RuO$_y$ clusters in oxygen exchange between nanocrystalline tin dioxide and the gas phase. *J. Phys. Chem. C* **2013**, *117*, 23858–23867. [CrossRef]

71. Descorme, C.; Duprez, D. Oxygen surface mobility and isotopic exchange on oxides: Role of the nature and the structure of metal particles. *Appl. Catal. A* **2000**, *202*, 231–241. [CrossRef]

72. Morrison, S.R. *The Chemical Physics of Surfaces*, 2nd ed.; Springer Science +Business Media, LLC: New York, NY, USA, 1990; pp. 29–31, ISBN 978-1-4899-2500-8.

73. Jaeckel, R.; Wagner, B. Photo-electric measurement of the work function of metals and its alteration after gas adsorption. *Vacuum* **1963**, *13*, 509–511. [CrossRef]

74. Ganose, A.M.; Scanlon, D.O. Band gap and work function tailoring of SnO_2 for improved transparent conducting ability in photovoltaic. *J. Mater. Chem. C* **2016**, *4*, 1467–1475. [CrossRef]

75. Lalik, E.; Kosydar, R.; Tokarz-Sobieraj, R.; Witko, M.; Szumełda, T.; Kołodziej, M.; Rojek, W.; Machej, T.; Bielańska, E.; Drelinkiewicz, A. Humidity induced deactivation of Al_2O_3 and SiO_2 supported Pd, Pt, Pd-Pt catalysts in $H_2 + O_2$ recombination reaction: The catalytic, microcalorimetric and DFT studies. *Appl. Catal. A* **2015**, *501*, 27–40. [CrossRef]

76. Degler, D.; Pereira de Carvalho, H.W.; Kvashnina, K.; Grunwaldt, J.-D.; Weimar, U.; Bârsan, N. Structure and chemistry of surface-doped $Pt:SnO_2$ gas sensing materials. *RSC Adv.* **2016**, *6*, 28149–28155. [CrossRef]

77. Michaelson, H.B. The work function of the elements and its periodicity. *J. Appl. Phys.* **1977**, *48*, 4729–4733. [CrossRef]

78. Benesh, G.A.; Liyanage, L.S.G. The surface electronic structure of oxygen on $Pt(001)(1 \times 1)$. *Surf. Sci.* **1992**, *261*, 207–216. [CrossRef]

79. Sales, B.C.; Turner, J.E.; Maple, B.M. Oscillatory oxidation of CO over Pt, Pd and Ir catalysts: Theory. *Surf. Sci.* **1982**, *114*, 381–394. [CrossRef]

80. Bârsan, N.; Rebholz, J.; Weimar, U. Conduction mechanism switch for SnO_2 based sensors during operation in application relevant conditions; implications for modeling of sensing. *Sens. Actuators B* **2015**, *207*, 455–459. [CrossRef]

81. Prasad, A.K.; Kubinski, D.J.; Gouma, P.I. Comparison of sol–gel and ion beam deposited MoO_3 thin film gas sensors for selective ammonia detection . *Sens. Actuators B* **2003**, *93*, 25–30. [CrossRef]

82. Korotcenkov, G.; Brinzari, V.; Golovanov, V.; Cerneavschi, A.; Matolin, V.; Todd, A. Acceptor-like behavior of reducing gases on the surface of *n*-type In_2O_3. *Appl. Surf. Sci.* **2004**, *227*, 122–131. [CrossRef]

83. Galatsis, K.; Cukrov, L.; Wlodarski, W.; McCormick, P.; Kalantar-zadeh, K.; Comini, E.; Sberveglieri, G. *p*- and *n*-type Fe-doped SnO_2 gas sensors fabricated by the mechanochemical processing technique. *Sens. Actuators B* **2003**, *93*, 562–565. [CrossRef]

84. Vorobyeva, N.; Rumyantseva, M.; Konstantinova, E.; Grishina, D.; Gaskov, A. Inversion of NH_3 sensor signal and paramagnetic centers of nanocrystalline ZnO(Ga). *Procedia Eng.* **2011**, *25*, 296–299. [CrossRef]

85. Shekunova, T.O.; Baranchikov, A.E.; Yapryntsev, A.D.; Rudakovskaya, P.G.; Ivanova, O.S.; Karavanova, Y.A.; Kalinina, M.A.; Rumyantseva, M.N.; Dorofeev, S.G.; Ivanov, V.K. Ultrasonic disintegration of tungsten trioxide pseudomorphs after ammonium paratungstate as a route for stable aqueous sols of nanocrystalline WO_3. *J. Mater. Sci.* **2018**, *53*, 1758–1768. [CrossRef]

86. Wu, Y.-Q.; Hu, M.; Wei, X.-Y. A study of transition from *n*- to *p*-type based on hexagonal WO_3 nanorods sensor. *Chin. Phys. B* **2014**, *23*, 40704. [CrossRef]

87. Kim, I.-D.; Rothschild, A.; Lee, B.H.; Kim, D.Y.; Jo, S.M.; Tuller, H.L. Ultrasensitive Chemiresistors Based on Electrospun TiO_2 Nanofibers. *Nano Lett.* **2006**, *6*, 2009–2013. [CrossRef] [PubMed]

88. Gurlo, A.; Sahm, M.; Oprea, A.; Barsan, N.; Weimar, U. A *p*- to *n*-transition on α-Fe_2O_3-based thick film sensors studied by conductance and work function change measurements. *Sens. Actuators B* **2004**, *102*, 291–298. [CrossRef]